

Simulation of four-dimensional CT images from deformable registration between inhale and exhale breath-hold CT scans

David Sarrut^{a)}

Centre Léon Bérard, Department of Radiotherapy, Lyon, France, LIRIS Laboratory, Université Lumière Lyon 2, Lyon, France, and CREATIS Laboratory, INSA — Bâtiment Blaise Pascal, 7, avenue Jean Capelle, 69621 Villeurbanne cedex, France

Vlad Boldea

LIRIS Laboratory, Université Lumière Lyon 2, Lyon, France, and Centre Léon Bérard, Department of Radiotherapy, Lyon, France

Serge Miguet

LIRIS Laboratory, Université Lumière Lyon 2, Lyon, France

Chantal Ginestet

Centre Léon Bérard, Department of Radiotherapy, Lyon, France

(Received 21 March 2005; accepted for publication 30 November 2005; published 9 February 2006)

Purpose: We propose to simulate an artificial four-dimensional (4-D) CT image of the thorax during breathing. It is performed by deformable registration of two CT scans acquired at inhale and exhale breath-hold. *Materials and methods:* Breath-hold images were acquired with the ABC (Active Breathing Coordinator) system. Dense deformable registrations were performed. The method was a minimization of the sum of squared differences (SSD) using an approximated second-order gradient. Gaussian and linear-elastic vector field regularizations were compared. A new preprocessing step, called *a priori* lung density modification (APLDM), was proposed to take into account lung density changes due to inspiration. It consisted of modulating the lung densities in one image according to the densities in the other, in order to make them comparable. Simulated 4-D images were then built by vector field interpolation and image resampling of the two initial CT images. A variation in the lung density was taken into account to generate intermediate artificial CT images. The Jacobian of the deformation was used to compute voxel values in Hounsfield units. The accuracy of the deformable registration was assessed by the spatial correspondence of anatomic landmarks located by experts. *Results:* APLDM produced statistically significantly better results than the reference method (registration without APLDM preprocessing). The mean (and standard deviation) of distances between automatically found landmark positions and landmarks set by experts were 2.7(1.1) mm with APLDM, and 6.3(3.8) mm without. Interexpert variability was 2.3(1.2) mm. The differences between Gaussian and linear elastic regularizations were not statistically significant. In the second experiment using 4-D images, the mean difference between automatic and manual landmark positions for intermediate CT images was 2.6(2.0) mm. *Conclusion:* The generation of 4-D CT images by deformable registration of inhale and exhale CT images is feasible. This can lower the dose needed for 4-D CT acquisitions or can help to correct 4-D acquisition artifacts. The 4-D CT model can be used to propagate contours, to compute a 4-D dose map, or to simulate CT acquisitions with an irregular breathing signal. It could serve as a basis for 4-D radiation therapy planning. Further work is needed to make the simulation more realistic by taking into account hysteresis and more complex voxel trajectories. © 2006 American Association of Physicists in Medicine. [DOI: 10.1118/1.2161409]

I. INTRODUCTION

Accounting for organ motion in lung cancer radiation treatment is an important challenge.¹ Breathing motion may be the source of several problems. It can lead to image artifacts such as distorted target volume.² Motion potentially leads to undercoverage of the Gross Tumor Volume (GTV) or unnecessary irradiation of healthy tissues. Reducing uncertainties on target position should result in a decrease in healthy lung irradiation and should allow tumor dose escalation, potentially leading to a better outcome.³

Respiratory motion during lung cancer radiation treatment can be addressed in several ways: margin adaptation, patient

breath-holding, gating, and tracking. The first approach consists of the defining of internal margins that take breathing motion into account. However, adjusting to the greatest tumor movement would increase healthy tissue irradiation, whereas defining too small margins might prevent adequate coverage of the GTV. The second approach consists of immobilizing the patient by controlled and reproducible apnea.⁴ It requires the evaluation of breath-hold reproducibility⁵ and that the patient understands and can follow the procedure. Gating consists of switching on irradiation when the target passes through the beam, and off when it moves out; it requires synchronization systems (such as Real-Time Position

Management, RPM, from Varian Medical Systems), reproducibility evaluation, and adapted dosimetry, taking into account residual motion. Tracking is the most ambitious process and requires specialized equipment and software. Ideally, tracking enables the beam to move along with the target.⁶

Whatever the approach, one needs patient-specific information about movements induced by breathing, and possibly by heartbeats,⁷ Several groups have recently proposed methods to acquire four-dimensional (4-D) CT scans.^{8–12} The 4-D images are reconstructed by synchronizing acquisition with an external (spirometer, RPM, thermometer) or internal (diaphragmatic cupola position^{13,14}) respiratory signal. Data are sorted according to a binning of the synchronizing signal and a 3-D image is reconstructed for each bin. Such techniques are not yet widely available. Another common way to acquire such motion information consists of acquiring several CT images at different breath-hold levels.^{15–17}

The 4-D images are not sufficient in themselves and should be associated with new image analysis tools.¹⁸ Ideally, treatment planning should not rely only on 3-D images, but also on a patient-specific breathing thorax model, encompassing all mechanical and functional information.¹⁹ Deformable registration algorithms can be used to automatically propagate 3-D organ or target delineation to all time-series images. They can also be used to build what we call a “4-D model,” composed of spatiotemporal trajectories of all volume elements in the thorax. Using such a model would contribute to better patient-adapted management of organ motion and would provide helpful information for planning real-time tracking and delivery.

In this paper, we propose a preliminary approach to build a 4-D breathing thorax model for a given patient. The model was built from CT scans acquired at exhale and inhale breath-holds, using image preprocessing, deformable registration, vector field interpolation, and image resampling with Jacobian-based generation of lung densities. This preliminary model does not yet include patient physiological properties nor mimic motion hysteresis, but could serve as a basis for more complex models.

II. PREVIOUS APPROACHES

This section is a review of several studies investigating deformable registration between CT images acquired at different breathing states. Readers interested in generic deformable registration methods can refer to Refs. 20 and 21. We will only focus on studies using deformable registration between CT thorax images: inhale/exhale breath-hold CT images, 3-D images of a 4-D CT scan, images acquired at various moments during the treatment for follow-up studies (see Ref. 22), or interpatient thorax images (to build an atlas of the human body, for instance²³).

Generally, the deformation is computed iteratively. At each iteration, the current deformation is evaluated according to two quantitative measures: a dissimilarity measure and a regularization measure. Low dissimilarity values indicate that the reference image is close to the current deformation

image (high values indicate that this is not the case). There are two main types of dissimilarity measures: measures based on a sparse set of features and measures using statistical analysis on the grey level distribution. Regularization of the deformation is the process that ensures a spatial coherence of the displacement field. Low regularization values indicate that the deformation is smooth or well-behaved. Regularization can be performed by including constraints on the vector fields, in order to penalize vector fields having neighboring voxels with motions in opposite directions, for instance; or an intrinsically smooth deformation field can be obtained by using different types of splines.^{16,23–25}

Several groups used sparse sets of anatomical features (mostly selected points or extracted surfaces) in each image, established pairs of correspondences between features, and finally computed a dense displacement field with an interpolation model based on the paired features.^{26,27,23,28,16,24,22} In Refs. 26, 27, and 16, features were points manually located and paired by experts. Experts successfully established correspondence between sets of points, even when interobserver variability was taken into account, but it is a time-consuming, error prone process that is not appropriate for daily use. In Ref. 24, features were automatically determined using the image gradient and, in Ref. 22, using slice by slice segmentation. Methods employing automatic feature selection face the difficulties of (1) establishing a correspondence between landmarks and (2) ensuring that the extracted landmarks in the two images correspond to the same physical points. Moreover, landmarks should be uniformly distributed within the volume, in order to correctly infer the deformation. Warping models used to compute dense displacement fields were as follows: thin-plate spline^{16,23} with inverse-consistent constraints,²³ radial basis interpolation with the shift log function,²² and B spline.²⁴ Table I summarizes the different types of landmarks that have been used.

An alternative class of methods relies on dense intensity-based similarity measures. Most authors^{27,29,23,30,31,25} used the sum of squared intensity differences (SSD; see Sec. IV C) or the sum of intensity differences (SID) for measuring dissimilarity and neglected the variations of lung density due to breathing. Sundaram *et al.*³² used normalized cross-correlation (CC) on 2-D MRI slices, Coselmon¹⁶ used mutual information (MI) on right lung images, Weruaga *et al.*²⁹ computed a similarity measure that was a combination of CC and SSD. All these (dis)similarity measures potentially took into account the change in lung density due to inspiration, but this was not studied by the authors. However, such approaches required the computation of the similarity measure over the neighborhood of each point, while SSD is a voxel to voxel measure. Table II summarizes some characteristics of deformable registration methods used for thorax CT analysis.

To our knowledge, no study has addressed intermediate organ positions throughout the breathing process or compared results with and without taking into account changes in lung density. Motion can be visualize using 4-D CT images and successive deformations between 3-D image time series. However, 4-D CT scans are not widely available and further work is needed to merge successive deformable registrations

TABLE I. Types of landmarks used for thorax CT registration (BH CT=breath-Hold Computerized Tomography; FU CT=follow-up CT acquired on the same patient at several weeks intervals; VC=vital capacity; IMSP=iterative most similar point; SOM=self-organizing map).

References	Types of features	Selection	Pairing	Numbers	Images
Fan <i>et al.</i> , 2001 (Ref. 27)	Bronchial points of airway trees and vessels+lungs surfaces	Manual for points and auto for lung surface	Manual	5 to 6 features points on each slice	BHCT at 40% and 75% of the VC
Li <i>et al.</i> , 2003 (Ref. 23)	Branch of the pulmonary airway tree	Auto (airway tree segmentation and thinning)	Manual	10–15 points	BH CT interpatient (85% VC)
Betke <i>et al.</i> , 2003 (Ref. 28)	Sternum, vertebra, trachea	Auto (templates based)	Template-based method	80 landmarks	FU CT (affine registration)
Coselmon <i>et al.</i> , 2004 (Ref. 16)	Right lung, in exhale image	Manual (roughly)	Semiauto	30 points on right lung (5–6 by slices)	BH CT at the end of normal inhale/exhale
Stewart <i>et al.</i> , 2004 (Ref. 24)	Points according to image gradient characteristics	Auto (image gradient)	Auto (IMSP)		FU CT, CT from 4-D CT
Matsopoulos <i>et al.</i> , 2005 (Ref. 22)	Vertebral spine, thoracic ribs and shoulder blades	Auto (slice by slice segmentation)	Auto (SOM)	About 500 points	FU CT

TABLE II. Characteristics of some dense deformable registration methods used for thorax CT registration (SSD=sum of squared intensity differences; SID=sum of intensity differences; CC=cross-correlation; OFC=optical flow constraint; MI=Mutual information; TPS=thin-plate spline; BH-CT=breath-hold CT; MRI=magnetic resonance imaging).

Reference	Similarity measure	Regularization/warping model	Resolution	Images
Fan <i>et al.</i> , 2001 (Ref. 27)	SSD (OFC)	Optical flow constraint+ anisotropic smoothness+divergence free	Gradient descent	BH CT inhale/exhale
Weruaga <i>et al.</i> , 2003 (Ref. 29)	Combination of CC+SID	Parametric models and smooth regularization adapted from snake	Fitting and filtering	BH CT inhale/exhale
Li <i>et al.</i> , 2003 (Ref. 23)	Consistent SSD	Consistent TPS	Gradient descent (alternate with landmark)	BH CT inter-patient
Lu <i>et al.</i> , 2004 (Ref. 30)	SSD (OFC)	Frobenius norm on Jacobian matrix	Gauss-Seidel finite difference	BH CT inhale/exhale
Guerrero <i>et al.</i> , 2004 (Ref. 31)	SSD (OFC)	Frobenius norm on Jacobian matrix	Gradient descent	BH CT inhale/exhale
Kaus <i>et al.</i> , 2004 (Ref. 25)	SSD	B spline	Levenberg-Marquardt	4DCT
Coselmon <i>et al.</i> , 2004 (Ref. 16)	MI	TPS	Iterative with control points	BH CT inhale/exhale
Sarrut <i>et al.</i> , 2005 (Ref. 5)	SSD (second-order gradient)	Gaussian	Gradient descent	BH CT (~ same volume)
Sundaram <i>et al.</i> , 2005 (Ref. 32)	CC	Linear elastic (fluid)	Gradient descent	MRI 2D
This work	SSD (second-order gradient)+APLDM	Gaussian and linear elastic (fluid)	Gradient descent	BH CT inhale/exhale

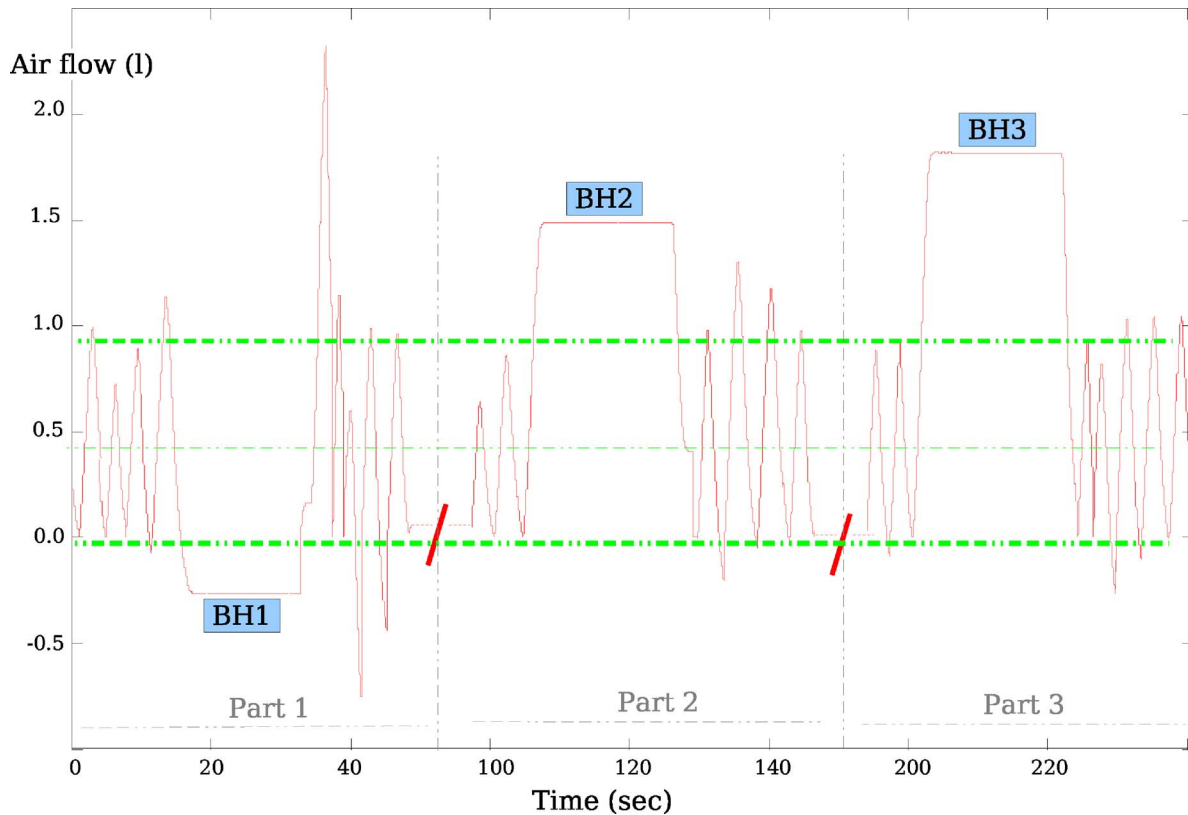


FIG. 1. Concatenation of three parts of an ABC (air flow) signal. Each part shows a short period of normal breathing followed by a breath-hold of about 20 s. The three breath-hold levels correspond to about $0.2L$ below normal expiration (exhale, denoted BH1), $0.2L$ above normal inspiration (inhale, BH2) and 70% of the total capacity (BH3). The three horizontal lines delimit the end, the beginning, and the mean of normal respiration.

into a single, consistent 4-D deformable model. In this study, we propose an image processing technique that takes into account the changes in lung densities during the deformable registration, and we outline a method for generating artificial intermediate CT images.

III. MATERIAL

We used images from patients enrolled in a clinical study initiated at our institution (a study approved by the local ethics committee according to French law). For each patient, three CT image sets were acquired in breath-hold. Active breath-holding was implemented with Active Breathing Control (ABC) device, developed by Wong *et al.*³³ and commercialized by Elekta[®]. ABC immobilizes a patient's breath during acquisition at a predefined respiratory level controlled by a digital spirometer. The three image sets were acquired at about $0.2L$ below normal expiration (BH1), about $0.2L$ above normal inspiration (BH2) and at 70% of the total lung capacity (BH3), according to patient ability. The dataset was composed of 3-D images of size 512×512 with 60–70 slices and $0.9 \times 0.9 \times 5$ mm³ voxels. In this study we studied four datasets. Functional lung information such as vital capacity, residual functional capacity, and compliance was available for each patient. Finally, for each CT image acquisition, the air-time signal was recorded by the ABC device. The signal corresponded to the airflow (in liters) as a function of time (in seconds), at a rate of 1/50 s. Figure 1 depicts

the three parts of the signal. Each part shows a short period of free breathing, followed by a breath-hold of about 20 s.

IV. METHOD

The proposed method involved four main steps. (I) Pre-processing consisted of segmenting the 3-D images into three regions labeled as air, patient, and lung. (II) We performed an *a priori* lung density modification in order to take into account the density decrease due to inhalation. (III) A dense deformation field between two CT images was then computed by using an optical-flow-like approach, adapted for large deformations. (IV) The last step consisted of generating intermediate deformation fields by linear interpolation and generating intermediate 3-D CT images by backward warping and Jacobian-based lung density generation.

A. Step I: Image preprocessing

Preprocessing steps consisted of identifying voxels that did not belong to the patient (air, table) and removing them from images. This was done by thresholding and morphological operations.⁵ Voxels outside the patient were attributed a Hounsfield value of -1000 (air density). Images were then rigidly registered in order to align as much as possible the rigid bony structures (spine). This was done by downsampling voxel intensities from 16 bits to 8 bits and by selecting intensities centered on bony structures. We used an imple-

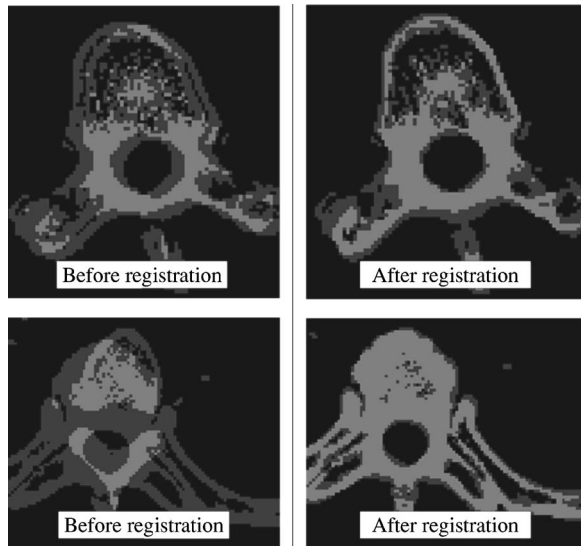


FIG. 2. Two examples of overlapping between segmented bony structures. Left images were taken before rigid registration and right images after. Overlapping areas are displayed in light grey and nonoverlapping areas in dark grey.

mentation of voxel-based rigid registration (based on Refs. 34 and 35) developed at our institution, using a correlation coefficient as the similarity measure and Powell–Brent as the optimization method. The quality of rigid registration was difficult to assess because images were not related by a rigid transformation. However, we checked that rigid structures were aligned by computing the overlap percentage of a segmented spine. The mean overlap was 64% between BH1–BH2 and 51% between BH1–BH3 before rigid registration, and, respectively, 74% and 84% after registration; see Fig. 2. We did not further investigate the validation of rigid registration because the accuracy of deformable registration is not sensitive to the rigid step's accuracy. When registered, images were resampled using the rigid transformation model and trilinear interpolation in order to have isotropic voxels.

B. Step II: *A priori* Lung Density Modification (APLDM)

The use of dissimilarity measures such as SSD leads to the assumption that point intensity is conserved from one image to another, but at a different location. This intensity conservation assumption is globally valid for each volume element outside the lungs because images are of the same modality. However, it is invalid inside the lung where the quantity of inspired air leads to a decrease of lung density. The density decrease is known to be distributed in the whole lung volume,³⁶ although it is more important in the lower parts of the lungs than in the upper parts;³⁷ indeed, regional specific thoracopulmonary compliance was found to increase with the lung distance from the lung apex. We thus proposed to artificially change the lung density of one image in order to be closer to the intensity conservation assumption.

The *a priori* precise knowledge of correct densities in the lungs is not possible because it would require knowing each

volume element's displacement, which is exactly what we are looking for. On the other hand, if the final density of each volume element was known, correct local norms of displacement could be computed. Let I_1 and I_2 be the two images to be registered. Let $\rho_1(z)$ and $\rho_2(z)$ denote the mean lung density of slice z . By identifying and pairing the first and last lung slices in the two images, we linearly related slice z in image I_1 with slice z' in image I_2 . Then, modifying density $I_1(\mathbf{x})$ of voxel \mathbf{x} belonging to slice z , by $I'_1(\mathbf{x}) = I_1(\mathbf{x}) + \rho_2(z') - \rho_1(z)$ allowed to artificially change lung densities of image I_1 according to those of I_2 . Images modified with this technique are called APLDM images.

C. Step III: Deformable registration schemes

Deformable registration between two images I_1 and I_2 is generally considered as the minimization of an energy function composed of a tradeoff between image dissimilarity and deformation regularity. We denoted by $\mathbf{u}(\mathbf{x})$ the displacement of a point \mathbf{x} and by $\phi(\mathbf{x}) = \mathbf{x} + \mathbf{u}(\mathbf{x})$ the related deformation. Dissimilarity was measured using the sum of squared differences (SSD), $SSD(I_1, I_2, \phi) = \sum_{\mathbf{x} \in \Omega} (I_1(\mathbf{x}) - I_2(\phi(\mathbf{x})))^2$ (with Ω the overlapping image domain). We used two types of regularization. The first one was Gaussian convolution²¹ of the vector field, denoted by G , because it is known to allow fast convergence for large displacements. It consists of the application of a 3-D Gaussian filter to the three components of the vector field, resulting in a smoother field. The second regularization was linear elastic²⁰ regularization that constrains the vector field to be close to the deformation of an elastic material, for which the force– displacement relationship is assumed to be linear.

As minimization was performed by a steepest gradient descent, the local gradient (i.e., the gradient of each point) of the SSD and the regularization had to be computed. For the gradient of the SSD, we used an expression, denoted by ∇L , proposed by Pennec *et al.*,³⁸ which limits the local displacement at each iteration according to a maximum vector displacement α [see Eq. (1)]. This criterion is an approximation of a second-order gradient descent of the SSD.³⁹ For small displacements, as is the case at each iteration, it is equivalent to express ∇L according to the gradient of image I_1 or of image I_2 (by inverting the transformation). It is, however, simpler and faster to use ∇I_1 because it does not require the computation of ∇I_2 at each iteration, unlike in Ref. 30. For one given voxel \mathbf{x} , the local iterative update schemes according to the two methods G (Gaussian) and LE (linear elastic) are expressed in Eq. (2) as proposed in Ref. 39, and Eq. (3) using steepest gradient descent:⁴⁰

$$\nabla L(\mathbf{x}, \mathbf{u}) = \frac{I_1(\mathbf{x}) - I_2(\mathbf{x} + \mathbf{u}(\mathbf{x}))}{\|\nabla I_1(\mathbf{x})\|^2 + \alpha^2 (I_1(\mathbf{x}) - I_2(\mathbf{x} + \mathbf{u}(\mathbf{x})))^2} \nabla I_1(\mathbf{x}), \quad (1)$$

$$(G) \quad \mathbf{u}_{i+1}(\mathbf{x}) = G_\sigma(\mathbf{u}_i(\mathbf{x}) + \nabla L(\mathbf{x}, \mathbf{u}_i)), \quad (2)$$

$$(LE) \quad \mathbf{u}_{i+1}(\mathbf{x}) = \mathbf{u}_i(\mathbf{x}) + \epsilon(\gamma \nabla L(\mathbf{x}, \mathbf{u}_i) + (1 - \gamma) \nabla LE(\mathbf{x}, \mathbf{u}_i)), \quad (3)$$

$$\nabla \text{LE}(\mathbf{x}, \mathbf{u}) = (1 - \xi) \nabla (\nabla \cdot \mathbf{u}(\mathbf{x})) + \xi \Delta \mathbf{u}(\mathbf{x}); \quad (4)$$

\mathbf{u}_i denotes the displacement field at iteration i , $\mathbf{u}(\mathbf{x})$ denotes the displacement at point \mathbf{x} , $\nabla I_1(\mathbf{x})$ denotes the gradient of image I_1 at point \mathbf{x} , $G_\sigma(\cdot)$ denotes Gaussian kernel of variance $\sigma > 0$ (large σ values smooth the vector field), $\text{LE}(\cdot)$ denotes linear-elastic regularization operator, γ denotes the tradeoff between image dissimilarity and regularization, and $\epsilon > 0$ denotes the gradient descent step. Large γ values increase the weight of image dissimilarity, while low values increase the weight of regularization ($\gamma \in [0:1]$). Large ϵ values could decrease the number of iterations required to converge, but also increase the possibility to get trapped in local minima. The gradient of linear elastic regularization is expressed in Eq. (4), with ξ ($\frac{1}{2} < \xi \leq 1$) denoting the tradeoff between the Laplacian and the gradient of divergence, as defined in Ref. 41. Low values of ξ are related to the lateral contraction due to longitudinal extension. Differential operators of the linear elastic regularization model were computed by finite differences. Gaussian filtering was performed using Deriche's recursive Gaussian filter.⁴²

D. Step IV: Intermediate image generation

We describe here a method to generate artificial CT images corresponding to intermediate breathing states, taking into account deformation fields between two inhale/exhale CT images. The goal of the first step is to generate intermediate deformation fields. The second step performs image warping with Jacobian-based density generation.

1. Intermediate deformation field

Computed vector fields described the start and end positions of each volume element (voxel) in the source image. To obtain the intermediate thorax position, we considered the linear pathway of each particle along its displacement vector, assuming that each particle displacement is along a straight line. Let \mathbf{u} be the displacement map that deforms image I_1 into image I_2 . Let $s \in [0, 1]$ denote the intermediate step between the two images. The intermediate displacement field corresponded to $\mathbf{u}_s = s\mathbf{u}$.

This is an approximation of real movements since we know that displacements are subject to hysteresis:⁴³ the inhalation pathway is different from the exhalation pathway. In Ref. 43, hysteresis was observed (on tumors) in 50% of cases (10 of 20 patients) and the amplitude was lower than 3 mm, except for one patient with 5 mm amplitude. According to the data presented in Ref. 43, we computed the ratio between hysteresis and displacement (see Table III). Results suggested that the major part of the displacement is not concerned with hysteresis (particularly for large displacements) and that lower parts of the lung show less hysteresis than upper parts, although this does not imply that displacement is close to a straight line). Non-straight-line displacement and the effect of hysteresis should not be neglected in the future, particularly for upper parts of the lung.

TABLE III. Ratio between hysteresis and displacement (in mm) determined as in Ref. 43. The last column indicates the location of the measured point.

Patient	Magnitude of 3-D displacement	Hysteresis norm	Ratio	Lobe
20	24.7	1.0	4%	Lower
9a	13.6	2.0	15%	Lower
10	12.2	2.0	16%	Lower
19	12.6	3.0	24%	Middle
12	6.0	2.0	33%	Upper
8	12.0	5.0	42%	Upper
1	4.2	2.1	49%	Upper
11	3.3	1.8	54%	Upper
2	2.9	1.8	63%	Upper
15	3.4	2.5	73%	Upper
9b	4.8	3.6	75%	Upper

2. Jacobian-based intermediate voxel density generation (JBDG)

For a given intermediate displacement field \mathbf{u}_s computed between two images I_1 and I_2 , simple image warping would not take into account the density change due to the variation in air volume. Generating intermediate lung densities is possible by interpolating start and end densities. For that, we need to know the inverse of the deformation (when inversion is possible) or the two deformation fields between I_1 and I_2 , using alternatively each image as a reference. We also proposed to compute local lung densities according to local volume change due to the deformation.

Let ϕ denote a deformation field computed between images I_1 (reference) and I_2 . Reverse mapping makes it possible to warp intensities of image I_2 and obtain an I_1 -like image.³⁹ Note that ϕ was computed from I_1 to I_2 , but it was I_2 , which was deformed by (implicitly) the inverse of the deformation. Let v_2 denote an initial volume in I_2 with initial density ρ_2 , and v_1 denote the final volume obtained after deformation. We are looking for final density ρ_1 , expressed in Hounsfield units, $\text{HU}_1 = 1000[(\rho_1 - \rho_w)/(\rho_w - \rho_a)]$ with ρ_w the water density and ρ_a the air density (inferred by an estimation of the Hounsfield units of air and water on the images²⁷). A local volume change due to the deformation could be approximated from the determinant of the Jacobian of the deformation field:⁴⁴ $v_2/v_1 \approx \det(\nabla \phi) = \det(\nabla \mathbf{u} + \text{Id})$ (with Id the identity matrix). The only difference between two lung states is the volume of air. Irrespective of the mass of air (because ρ_a is close to 0), the masses of the two volumes v_1 and v_2 are identical: $\rho_1 v_1 = \rho_2 v_2$. Thus, we have $\rho_1 = \rho_2(v_2/v_1)$. In Hounsfield units, we get (with $\rho_a = 0$ and $\rho_w = 1$)

$$\text{HU}_1 = \det(\nabla \phi)(1000 + \text{HU}_2) - 1000. \quad (5)$$

Finally, the warped image can be computed by reverse mapping of $\phi(I_2)$ values, converted according to Eq. (5).

3. Temporal sequence

The intermediate states do not form a temporal sequence because index s does not refer to a temporal dimension but to

an intermediate position. To relate index s to a temporal deformation (indexed by t), we used the airflow signal available from the ABC device, denoted $\text{Flow}_{\text{air}}(t)$, that gives inhaled air volume as a function of time. For a given s , we computed the corresponding lung air volume, denoted by $\text{Vol}_{\text{air}}(\mathbf{u}_s) = V_s$, from the generated intermediate image. Then, the intermediate image was associated with time t such that $\text{Flow}_{\text{air}}(t) - \text{Flow}_{\text{air}}(\text{ref}) = V_s - V_{\text{ref}}$, with $\text{Flow}_{\text{air}}(\text{ref})$ and V_{ref} the air flow and volume corresponding to image I_1 . The percentage of air volume inside the regional lung was computed as in Ref. 27 [Eq. (6)], where the relation between Hounsfield units and densities of air and water is considered linear. For any temporal breathing signal, it was thus possible to associate each intermediate step s with a time step t ,

$$\% \text{air} = 1 - \frac{\text{HU} - \text{HU}_{\text{air}}}{\text{HU}_{\text{water}} - \text{HU}_{\text{air}}}. \quad (6)$$

V. EXPERIMENTS AND RESULTS

A. Experimental setup

Several registrations were performed in order to compare and evaluate the methods: with and without APLDM, with Gaussian or linear elastic regularization. Trilinear interpolation was used throughout the different steps. The number of iterations for Gaussian regularization was empirically set to 3000 (after convergence) in order to compare results. Linear elastic regularization was performed after Gaussian regularization using 1000 supplementary iterations because convergence using Gaussian is faster at the first steps of the registration.⁴⁰ Results obtained when using linear elastic from the first iteration were similar to those obtained using Gaussian, then linear elastic regularization, but this required substantially more iterations. Maximum vector displacement α , Eq. (1), was set to 1.0 voxel. The variance of Gaussian regularization was $\sigma = 1.0$. For linear elastic, γ was set to 0.5, ϵ to 0.1, and ξ to 0.6.

Registrations were performed according to the same reference (breath-hold at maximal lung volume, BH3–BH1, BH2–BH1, BH3–BH2) for four different patients. The registrations correspond to different magnitudes of deformation: BH3–BH1 and BH2–BH1 were large deformations (lung volume increase by, respectively, 162% and 151%; larger displacements of about 30 mm), whereas BH3–BH2 were small deformations (108%). We did not study registration consistency; interested readers can refer to Refs. 40 and 20. Images and computed vector fields were sampled at $2.5 \times 2.5 \times 2.5 \text{ mm}^3$, leading to an image size of about $200 \times 200 \times 120$ voxels (4.8 million voxels). We obtained a total of 48 deformation fields.

B. Validation with expert landmarks

1. Material and method

Anatomical landmarks inside the lungs were manually selected and labeled in each image by four experts (a lung specialist, a physician, and two physicists). For each patient, the first expert determined a reference set of landmarks in

each image, with the following instructions: each landmark should be undoubtedly identifiable and labeled with a descriptive name, allowing other experts to find it; the landmarks should be spread as uniformly as possible throughout the lungs (in left/right lung, upper/lower, and central/peripheral part of the lungs). Between 14 and 25 image points were selected, corresponding to the carina, calcified nodules, culmen-lingula junction, division branch of pulmonary artery, apical pulmonary vein of upper lobe, for instance.

These landmarks were then located in the two other images by all the experts. Let \mathbf{p}_i^e denote a landmark location in image I_i , selected by expert e . The four locations of the point were averaged to define a pseudoground truth landmark denoted by $\mathbf{q}_i = \frac{1}{4} \sum_e \mathbf{p}_i^e$. In order to evaluate the variability associated with the manual identification of anatomical landmarks by observers, we computed the mean and the standard deviation of the distances between all \mathbf{q}_i and all \mathbf{p}_i^e . Let I_1 and I_2 be two images to be registered. For each \mathbf{q}_1 in reference image I_1 , we computed its location \mathbf{r}_2 in I_2 using the displacement field \mathbf{u} computed between I_1 and I_2 : $\mathbf{r}_2 = \mathbf{q}_1 + \mathbf{u}(\mathbf{q}_1)$. Distances d_2 between the reference landmark \mathbf{q}_2 and the estimated landmark \mathbf{r}_2 were then computed: $d_2 = \sqrt{(\mathbf{q}_2 - \mathbf{r}_2)^2}$.

2. Precision of manual landmark selection

The task of manually selecting landmarks was time consuming and was considered tedious by experts. The selection of landmarks in end-expiration images was also considered more difficult because of tissue thickening. Interobserver variability, characterized by the mean and standard deviation of all distances between all \mathbf{q}_i and all \mathbf{p}_i^e , was 2.3(1.2) mm or 1.6(0.9) voxels. Distances d_i are displayed in Table IV. An example of landmark positions is shown in Fig. 3.

3. Jacobian of the deformation field

We also computed the percentage of points with a negative Jacobian in each deformation field. A negative Jacobian means that the deformation is locally noninvertible and is an indicator of the locally bad estimation of the deformation.⁴⁴ Table V shows the mean percentage of volume elements with a negative Jacobian and indicates whether differences between methods were or not statistically significant.

4. Conclusion

Both criteria (the distance between landmarks, negative Jacobian) lead to two similar conclusions: (1) deformable registration performed better with APLDM than without, and (2) the difference between Gaussian and linear elastic regularization was not statistically significant. Registrations with APLDM provided superior accuracy, with 2.7(1.1) mm mean and standard deviation for Gaussian and large deformation, versus 6.3(3.8) mm without APLDM. The difference was statistically significant for large deformations (BH3–BH1 and BH2–BH1, $p = 0.001$) and not significant for small deformations (BH3–BH2). This accuracy was similar to the inter-

TABLE IV. Mean of distances between reference and estimated landmark positions for the initial pairs of images (column “initial distance”) and for each deformable registration: with and without A Priori Lung Density Modification (APLDM) method, with Gaussian (G), or linear elastic (LE) regularization methods. Distances are expressed in millimeters in the left table and in voxels in the right table (computed according to the anisotropic resolution of the voxel in initial images).

	Distances are in millimeters					Distances are in voxels				
	Initial distance	Without APLDM		APLDM		Initial distance	Without APLDM		APLDM	
		G	LE	G	LE		G	LE	G	LE
BH3–BH1										
P1	16.5	7.6	7.6	2.1	2.2	16.0	6.4	6.1	2.1	2.0
P2	15.1	10.2	9.0	3.7	3.5	5.4	7.2	6.4	2.3	2.3
P3	23.8	8.4	8.6	4.2	5.0	22.7	7.0	6.7	3.6	3.7
P4	17.6	11.7	8.8	3.6	4.2	13.2	11.6	8.3	3.0	3.6
Mean	18.2	9.5	8.5	3.4	3.7	14.3	8.0	6.9	2.7	2.9
Stdev	3.8	1.8	0.6	0.9	1.2	7.2	2.4	1.0	0.7	0.9
BH2–BH1										
P1	16.2	7.4	7.2	2.0	1.9	13.3	6.2	5.9	1.7	1.6
P2	11.0	6.2	5.7	1.6	1.8	5.1	5.0	4.6	1.3	1.3
P3	20.6	5.5	6.5	4.4	4.8	20.5	4.8	6.0	3.3	3.5
P4	13.8	11.5	8.6	3.7	4.6	11.7	11.3	8.4	3.3	4.2
Mean	15.4	7.6	7.0	2.9	3.3	12.7	6.8	6.2	2.4	2.7
Stdev	4.1	2.7	1.2	1.3	1.6	6.3	3.1	1.6	1.1	1.4
BH3–BH2										
P1	5.8	2.2	2.3	2.2	2.3	3.7	1.6	1.6	1.6	1.6
P2	4.8	1.7	1.9	1.8	2.0	1.3	1.3	1.5	1.2	1.4
P3	6.8	1.8	1.8	1.7	1.8	3.1	1.0	1.0	1.1	1.1
P4	5.2	1.9	1.8	1.8	1.8	2.4	1.4	1.2	1.2	1.1
Mean	5.6	1.9	2.0	1.9	2.0	2.6	1.3	1.3	1.3	1.3
Stdev	0.9	0.2	0.2	0.2	0.2	1.1	0.2	0.3	0.2	0.3
Total										
Mean	13.1	6.3	5.8	2.7	3.0	9.9	5.4	4.8	2.1	2.3
Stdev	6.4	3.8	3.0	1.1	1.3	7.4	3.7	2.8	0.9	1.1

expert variability (2.3 mm). Gaussian and linear elastic regularizations led to similar results (differences were not statistically significant). APLDM led to significantly fewer points with negative Jacobian values ($p < 0.002$). Gaussian regularization led to fewer points with negative Jacobian values than linear elastic regularization, but this result was not statistically significant.

For five landmarks (over 60 points), distances d_i were larger than 10 mm (maximum was 15 mm), clearly indicating that the deformable field was badly estimated locally. This was probably due to the high differences between lung densities in parts of the lung due to the increased air volume and to the presence of emphysema bubbles. Further work is needed to investigate these situations and to automatically detect and correct them. Images warping with deformation fields generated with or without APLDM achieved comparable visual results, except in some lung locations, provided that the mode of intensity scaling was carefully selected (see Fig. 4). However, we observed that the deformation fields

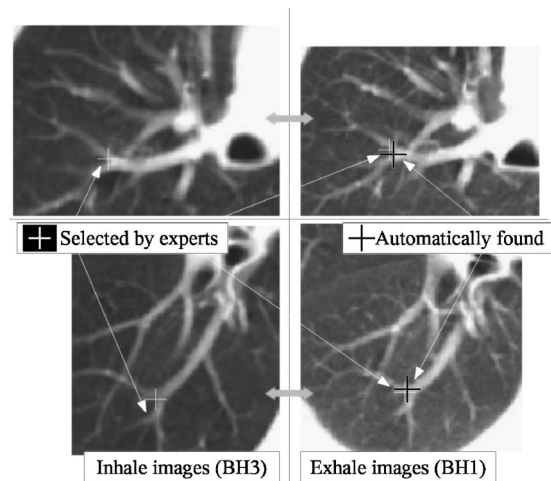


FIG. 3. Slices from BH3 (inhale, on the left) and BH1 (exhale, on the right). Examples of (pseudoground truth) landmarks selected by experts are marked with a white cross. Black positions were obtained by applying a deformable field to the white positions within images on the left.

TABLE V. Mean percentage of negative Jacobian (averaged on all patients). A comparison between pairs of methods: with/without APLDM, G/LE. The last column indicates whether the differences were statistically significant or not (paired t tests).

	BH3–BH1	BH2–BH1	BH3–BH2	Mean	Signific.
With APLDM	2.4%	1.4%	0.3%	1.4%	Yes
Without APLDM	4.4%	3.0%	0.4%	2.6%	$p < 0.002$
Gaussian	3.2%	1.9%	0.3%	1.8%	
Linear elastic	3.7%	2.4%	0.4%	2.2%	no

themselves were different (see Fig. 5): discontinuities existed without APLDM and disappeared when using it. The mean (standard deviation) of norms of the vector field differences was about 9.1(5.2) mm [or 3.6(2.0) voxels]. Differences were mostly located in the lung periphery.

C. Artificially generated intermediate image

1. Materials and methods

Our goal was to evaluate artificially generated intermediate images. We used a 4-D CT dataset acquired using a protocol similar to the one described in Ref. 10. This 4-D dataset was composed of ten 3-D CT images acquired at different phases of the respiratory cycle, from the end of normal inspiration to the end of normal expiration. All 3-D CT images were taken with the following resolution: $512 \times 512 \times 88$, with a voxel size of $0.97 \times 0.97 \times 2.5 \text{ mm}^3$. They were downsampled to an isotropic voxel size of 2.5^3 mm^3 . From the two extrema 3-D images (denoted I_I for end-inspiration and I_E for end-expiration), we generated two initial deformation fields (with APLDM), denoted by ϕ_{IE} and ϕ_{EI} , taking alternatively each image as a reference. According to the method described in Sec. IV D, we generated intermediate vector fields and intermediate images. Vector

fields were evaluated by a using expert-selected landmarks and images were evaluated by a voxel-based comparison with 3-D images available in the reference 4-D dataset.

(a) **Intermediate vector fields.** A physician selected 25 landmark points (a similar protocol as in Sec. V B) in four images: I_E , I_I , and two intermediate images denoted by I_1 and I_2 , corresponding to intermediate lung volumes (lung volumes for I_E , I_1 , I_2 , and I_I were, respectively, 4315, 4692, 5004, and 5181 cm^3). Let \mathbf{p} be a landmark and \mathbf{p}_E , \mathbf{p}_1 , \mathbf{p}_2 , and \mathbf{p}_I its positions in images I_E , I_1 , I_2 , and I_I .

We first computed the shortest distance, denoted by l_i , between \mathbf{p}_i (with $i=\{1,2\}$) and the line segment defined by \mathbf{p}_I and \mathbf{p}_E . Low values of l_i indicated that the displacement of the landmark was close to a straight line (as we assumed in Sec. IV D 1). Our assumption not only implies that the landmarks were close to the \mathbf{p}_E to \mathbf{p}_I line, with each $\mathbf{p}_i \approx \mathbf{p}_I + k_i(\mathbf{p}_E - \mathbf{p}_I)$, but also that the factor k_i was the same for all points (see Fig. 6). Landmarks \mathbf{p}_I were then warped according to the intermediate vector field, and we compared the new warped positions \mathbf{p}_i^* to the reference positions \mathbf{p}_i .

(b) **Intermediate warped images.** Intermediate deformation fields ϕ_s were computed such that warped images have approximately the same lung volume as the intermediate images. We used the sum of absolute differences (SAD) as a quality measure between warped I_i^* and reference I_i images: $\text{SAD}(I_i^*, I_i) = \sum_{\mathbf{x} \in \Omega} |I_i^*(\mathbf{x}) - I_i(\mathbf{x})|$, with Ω the overlapping region of the lung areas. Points with a negative Jacobian (less than 1.3%) were removed from the SAD computation. We tested three methods to generate intermediate images: with or without JBDG, and by combining two vector fields by linear interpolation between images warped with ϕ_{IE} and with ϕ_{EI} (see Sec. IV D 2).

2. Results

Distances between landmarks in image I_1 and landmarks in other images (I_E , I_1 , and I_2) are displayed in Table VI.

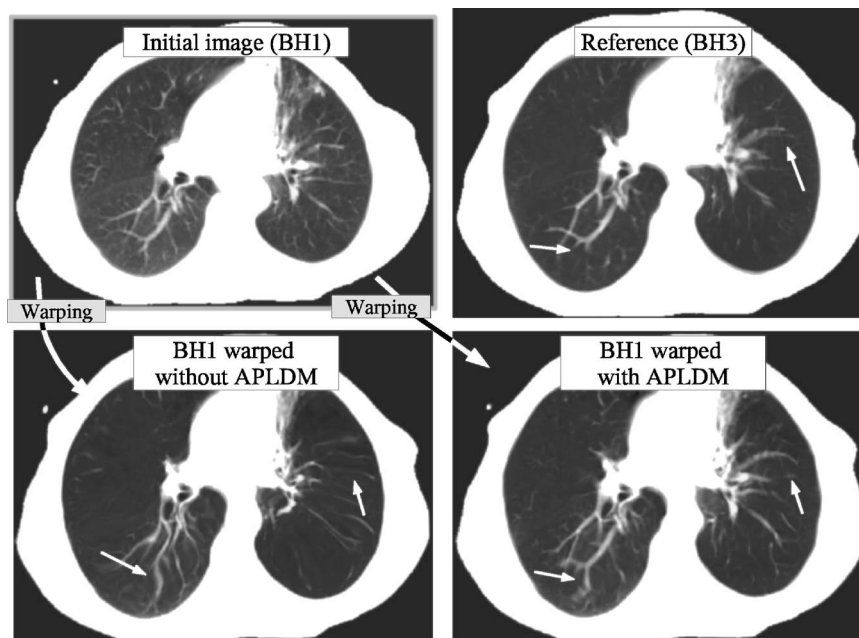


FIG. 4. A comparison between the reference image (BH3) and warped images $[\phi(BH1)]$ obtained from deformation fields with and without the APLDM method. Images are displayed with a grey scale that enhances the intensities in the lungs. The displayed slice was selected to focus on the differences between the two methods: white arrows indicate regions with visible differences.

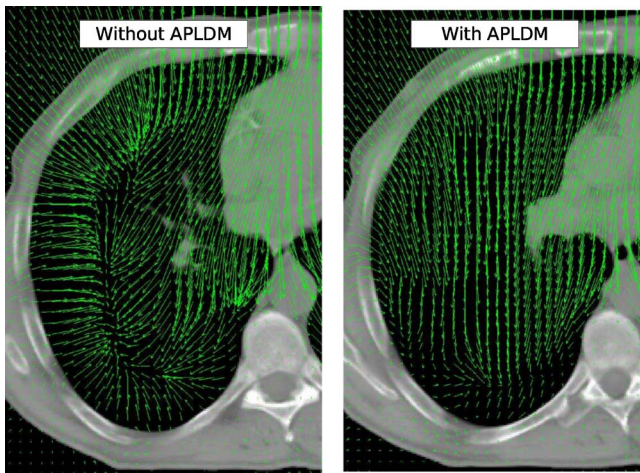


FIG. 5. Deformation fields superimposed on an axial slice. Deformations represent lung contraction between inhale and exhale images. The left field was computed without APLDM and right field with APLDM. For display purpose, displacement vectors are shown every 6 mm.

Only four of 50 intermediate point positions have distances greater than 4 mm. Distances l and factors k are also indicated (see Sec. V C 1). The mean of SAD rates between artificial images I_1^* and I_2^* and reference images I_1 and I_2 are displayed in Table VII.

3. Conclusion

The accuracy of the initial deformation (between I_1 and I_E) was 2.1(1.4) mm, which was similar to the one reported above (Sec. V B). Distances l_i were small (1.3 mm), indicating that the straight-line assumption was globally valid. However, the relatively high standard deviation of the k_2 factor (0.3) suggested that, even if landmarks seem to follow a straight-line path, a single k cannot be used for all voxels. For example, it should be possible to compute a parameter k for each voxel according to an *a priori* displacement speed derived from a physiological study. For intermediate images, the accuracy was of the same order as for the initial registration [2.6(1.7) mm]. The JBDG method only slightly improved image warping. Better results were obtained by using linear interpolation between warped images with ϕ_{IE} and with ϕ_{EI} , but this requires the computation of two vector fields. This will be investigated in the future. Figure 7 illustrates artificial intermediate images.

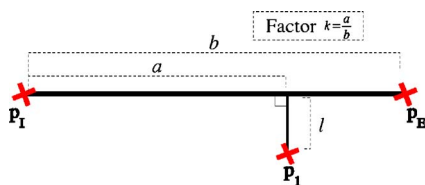


FIG. 6. \mathbf{p}_E , \mathbf{p}_1 , and \mathbf{p}_I positions of landmark \mathbf{p} are shown. l denotes the distance between \mathbf{p}_1 and the line segment defined by \mathbf{p}_I and \mathbf{p}_E . Factor k is the ratio between segment length [$b = \sqrt{(\mathbf{p}_E - \mathbf{p}_I)^2}$] and distance a from \mathbf{p}_I to the projection of \mathbf{p}_1 on the segment.

TABLE VI. The first two lines display the means (and standard deviation) of distances between landmarks in image I_I and landmarks in images I_E , I_1 , and I_2 , before and after registration. Distances are expressed in millimeters. The last two lines display the mean of distances l and of factors k .

Distances in mm	I_E	I_1	I_2
before registration	10.6(5.5)	7.8(4.6)	4.4(3.4)
after registration	2.1(1.4)	2.6(2.0)	2.7(1.5)
Mean of distance l	0	1.5(1.4)	1.2(0.8)
Mean of factor k	1	0.7(0.2)	0.4(0.3)

VI. DISCUSSION

Overall accuracy was clearly better with APLDM than without (2.7 vs 6.3 mm). However, we have only performed a global validation by averaging landmark distances. Validation on landmark positions does not necessarily imply that the deformation is correct everywhere inside the volume. Further validation should be performed to locally study deformation. Moreover, intensity-based deformation registration is sensitive to image quality: acquisition artifacts may induce locally imprecise or wrong deformation.

Interpolation of vector fields relied on assumptions that were not strictly satisfied such as straight line displacement or the absence of hysteresis. Displacements around the heart region were not taken into account. Nevertheless, the model simulated the major part of the displacement as the distance between landmarks and straight-line path was small (1.3 mm). Intermediate density generation was found to be slightly better with JBDG than without. Bilinear interpolation using two vector fields led to better results, but required twice as much time. We used 4-D CT acquired data because we wanted to compare a synthetic 4-D image with an acquired one. It allows a test of the proposed method with realistic deformation amplitudes. However, the differences between a static breath-hold image and a corresponding image (with the same lung volume) extracted from a dynamic 4-D dataset, are not well known (e.g., hysteresis, 4-D reconstruction). It would be interesting to compare breath-hold images and 4-D CT images of the same patient.

No particular effort has been made regarding computation times. Preprocessing took about 2–3 min, APLDM was quasi-instantaneous, and intermediate image generation took a few seconds. The computation time of deformable registrations depends on the resolution of images and on the deformation amplitude, i.e., the number of iterations required to

TABLE VII. The column “before registration” displays the SAD (sum of absolute differences) computed between I_i (with $i=1,2$) and I_E . Other columns display the SAD between I_i and artificial I_i^* computed without JBDG (Jacobian-Based Density Generation), with JBDG, and with linear interpolation (LI). SAD is expressed in Hounsfield units.

	Before reg.	Without JBDG	With JBDG	LI
I_1	129	84	82	76
I_2	187	89	87	83

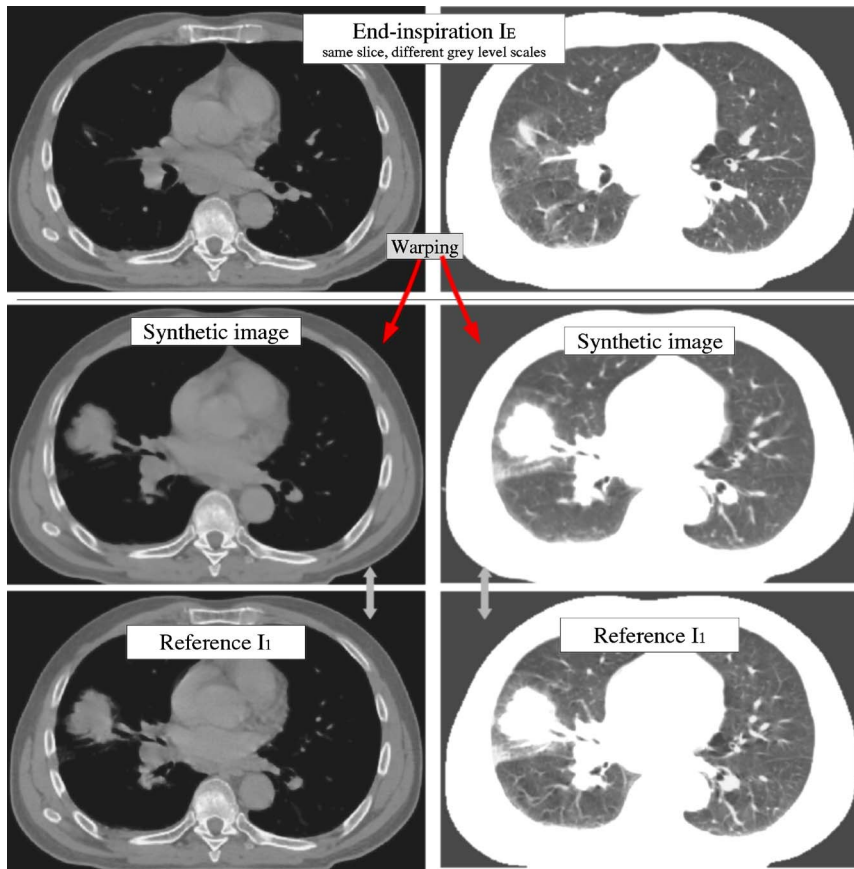


FIG. 7. A comparison between a reference image (I_1) and an artificial image (I_1^*). I_1^* was obtained by warping the initial image (I_E) using the JBDG method. The three images on the right are displayed with a grey scale that enhance the intensities in the lungs.

converge. Using a 2.8 Ghz PC with a 1 Gb RAM running Linux operating system, the computation time is about 1.5 s for one million voxels and for one iteration. For example, the registration of a whole thorax (about 45000 cm³ took 3 min with 5³ mm³ voxel size and 1000 iterations (medium deformation), or 1 h for 3³ mm³ voxel size and 4000 iterations (a very large deformation).

It should be stressed that the straight-line approach is a first step in building a 4-D model of the thorax. Further models will include more detailed motion parameters, such as lung hysteresis, temporal regularization, physiological information. However, it is important that the model remains driven by the patient's images in order to be adapted to each patient's characteristics. Compared to 4-D acquisition, building a 4-D model based on only two CT acquisitions can lower the imaging dose. Moreover, using such a model should help reduce image motion artifacts still present in current 4-D acquisitions.¹⁸

The advantages of a using *4-D model*, which not only includes a 4-D image but also provides a motion description, are the following. Organs and target contours can be automatically propagated at any given respiratory instant: drawing contours on several 3-D images is time consuming; our model would provide the users with initial contours that must be corrected only locally if needed. This approach still needs to be validated.

The 4-D model can also be used to estimate a 3-D dose map, taking into account respiratory motion. The respiratory

cycle is split into several instants, and a dose deposition calculation is performed on each instant using the same irradiation beam parameters. Then, the 3-D dose maps are merged into a single spatial reference by using the displacement map and temporal information of the 4-D model. It results in a 4-D map of the estimated dose deposition while the patient moves.

Some studies use the probability density function (PDF) of tumor presence to help define adequate margins.⁴⁵ Whereas the straight-line model remains a first-order approximation of real motion, a PDF can be automatically computed from the 4-D model for each voxel within a given region of interest, according to its own displacement amplitude and direction. The resulting PDF of a given region could be different from what would be obtained by using a single PDF for all voxels, with two extreme positions (end inhale, end exhale). Moreover, the 4-D model can help simulate any type of irregular breathing pattern (by choosing a given 1-D respiratory signal with irregularities in both amplitude and frequency) in order to generate an artificial 4-D image. The resulting 4-D image can be used, for example, to evaluate the robustness of a margin definition technique requiring regular breathing. We have already used this model to simulate free-breathing CT acquisitions using cone beam or helical CT for studying image-based respiratory signal extraction methods.¹⁴

VII. CONCLUSION

We have presented a method to compute a deformation field between inhale and exhale breath-hold CT images, taking into account changes of lung density. We have validated this approach by using landmarks manually selected by physicians. Global accuracy was better with APLDM than without (2.7 vs 6.3 mm) and close to the interobserver variability (2.3 mm). The number of points with a negative Jacobian was also statistically significantly lower. Linear elastic and Gaussian regularizations led to comparable results.

We also propose a method to create artificial intermediate CT images in order to simulate a 4-D CT model of the thorax. The model comprises the 4-D CT image, individual volume element displacement and deformation. The accuracy of intermediate vector fields was 2.6 mm. Jacobian-based lung density generation led to slightly better results than simple warping. Linear interpolation of two inverse deformation fields improved image resemblance.

Work is ongoing to enhance the performance of the APLDM method by alternating APLDM and deformable registration. We also aim at taking into account hysteresis and incorporating physiological information (such as lung compliance) into the model. We finally plan to use this 4-D model to help detect and remove 4-D acquisition artifacts by comparing 4-D acquisitions and simulated images.

ACKNOWLEDGMENTS

The authors thank Greg Sharp, Steve Jiang, and Noah Choi, from the Massachusetts General Hospital in Boston for providing us a 4-D CT dataset. The authors also wish to thank Dominique Arpin, Line Claude, and all other persons who have given their time to select landmark points.

^{a)} Author to whom correspondence should be addressed.. Department of Radiotherapy, Centre Léon Bérard, 28 rue Laennec, 69008 Lyon, France. Phone number: 33 4 78 78 51 51; Fax: 33 4 78 26 26. Electronic mail: David.Sarrut@creatis.insa-lyon.fr

¹ M. Goitein, "Organ and tumor motion: An overview," *Semin. Radiat. Oncol.* **14**, 2–9 (2004).

² G. Chen, J. H. Kung, and K. P. Beaudette, "Artifacts in computed tomography scanning of moving objects," *Semin. Radiat. Oncol.* **14**, 19–26 (2004).

³ C. C. Ling, E. Yorke, H. Amols, J. Mechalakos, Y. Erdi, S. Leibel, K. Rosenzweig, and A. Jackson, "High-tech will improve radiotherapy of NSCLC: a hypothesis waiting to be validated," *Int. J. Radiat. Oncol., Biol., Phys.* **60**, 3–7 (2004).

⁴ G. S. Mageras and E. Yorke, "Deep inspiration breath hold and respiratory gating strategies for reducing organ motion in radiation treatment," *Semin. Radiat. Oncol.* **14**, 65–75 (2004).

⁵ D. Sarrut, V. Boldea, M. Ayadi, J. N. Badel, C. Ginestet, and S. Clippe, "Non-rigid registration method to assess reproducibility of breath-holding with ABC in lung cancer," *Int. J. Radiat. Oncol., Biol., Phys.* **61**, 594–607 (2005).

⁶ M. Murphy, "Tracking moving organs in real time," *Semin. Radiat. Oncol.* **14**, 91–100 (2004).

⁷ M. Pollari, J. Lotjonen, T. Makela, N. Pauna, A. Reilhac, and P. Clarysse, "Evaluation of cardiac pet-mri registration methods using a numerical breathing phantom," in *International Symposium on Biomedical Imaging (ISBI): Macro to Nano*, IEEE Computer Society, Arlington, VA, 2004, pp. 1447–1450.

⁸ S. S. Vedam, P. J. Keall, V. R. Kini, H. Mostafavi, H. P. Shukla, and R. Mohan, "Acquiring a four-dimensional computed tomography dataset using an external respiratory signal," *Phys. Med. Biol.* **48**, 45–62 (2003).

⁹ P. Keall, "4-Dimensional computed tomography imaging and treatment planning," *Semin. Radiat. Oncol.* **14**, 81–90 (2004).

¹⁰ T. Pan, T. Y. Lee, E. Rietzel, and G. T. Chen, "4D-CT imaging of a volume influenced by respiratory motion on multi-slice CT," *Med. Phys.* **31**, 333–340 (2004).

¹¹ S. A. Nehmeh, Y. E. Erdi, T. Pan, A. Pevsner, K. E. Rosenzweig, E. Yorke, G. S. Mageras, H. Schoder, P. Vernon, O. Squire, H. Mostafavi, S. M. Larson, and J. L. Humm, "Four-dimensional (4–D) PET/CT imaging of the thorax," *Med. Phys.* **31**, 3179–3186 (2004).

¹² D. A. Low, M. Nystrom, E. Kalinin, P. Parikh, J. F. Dempsey, J. D. Bradley, S. H. Mutic, S. Wahab, T. Islam, G. Christensen, D. G. Politte, and B. R. Whiting, "A method for the reconstruction of four-dimensional synchronized CT scans acquired during free breathing," *Med. Phys.* **30**, 1254–1263 (2003).

¹³ J. J. Sonke, L. Zijp, P. Remeijer, and M. van Herk, "Respiratory correlated cone beam CT," *Med. Phys.* **32**, 1176–1186 (2005).

¹⁴ S. Rit, D. Sarrut, and C. Ginestet, "Respiratory signal extraction for 4D CT imaging of the thorax from cone-beam CT projections," in *Medical Image Computing and Computer-Assisted Intervention MICCAI'2005*, Lecture Notes in Computer Science, edited by J. S. Duncan and G. Gerig (Springer-Verlag, Berlin, 2005).

¹⁵ H. A. Shih, S. B. Jiang, K. M. Aljarrah, K. P. Doppke, and N. C. Choi, "Internal target volume determined with expansion margins beyond composite gross tumor volume in three-dimensional conformal radiotherapy for lung cancer," *Int. J. Radiat. Oncol., Biol., Phys.* **60**, 613–622 (2004).

¹⁶ M. M. Coselmon, J. M. Balter, D. L. McShan, and M. L. Kessler, "Mutual information based CT registration of the lung at exhale and inhale breathing states using thin-plate splines," *Med. Phys.* **31**, 2942–2948 (2004).

¹⁷ K. K. Brock, D. L. McShan, R. K. Ten Haken, S. J. Hollister, L. A. Dawson, and J. M. Balter, "Inclusion of organ deformation in dose calculations," *Med. Phys.* **30**, 290–295 (2003).

¹⁸ P. J. Keall, S. Joshi, S. S. Vedam, J. V. Siebers, V. R. Kini, and R. Mohan, "Four-dimensional radiotherapy planning for dmlc-based respiratory motion tracking," *Med. Phys.* **32**, 942–951 (2005).

¹⁹ P. F. Villard, M. Beuve, B. Shariat, V. Baudet, and F. Jaillet, "Lung mesh generation to simulate breathing motion with a finite element method," in *IEEE Conference on Information Visualization*, 14–16 July 2004, IEEE Computer Society, London, UK, 2004, pp. 194–199.

²⁰ G. E. Christensen and H. J. Johnson, "Consistent image registration," *IEEE Trans. Med. Imaging* **20**, 568–582 (2001).

²¹ J. P. Thirion, "Image matching as a diffusion process: an analogy with Maxwell's demons," *Med. Image Anal.* **2**, 243–260 (1998).

²² G. K. Matsopoulos, N. A. Mouravliansky, P. A. Asvestas, K. K. Delibasis, and V. Kouloulis, "Thoracic deformable, registration combining self-organizing maps and radial basis functions," *Med. Image Anal.* **9**, 237–254 (2005).

²³ B. Li, G. E. Christensen, E. A. Hoffman, G. McLennan, and J. M. Reinhardt, "Establishing a normative atlas of the human lung: intersubject warping and registration of volumetric CT images," *Acad. Radiol.* **10**, 255–265 (2003).

²⁴ C. V. Stewart, Y. L. Lee, and C. L. Tsai, "An uncertainty-driven hybrid of intensity-based and feature-based registration with application to retinal and lung CT images," in *Medical Image Computing and Computer-Assisted Intervention MICCAI'2004*, Lecture Notes in Computer Science, (Springer-Verlag, Berlin, 2004), Vol. 3217, pp. 870–877.

²⁵ M. R. Kaus, T. Netsch, S. Kabus, V. Pekar, T. McNutt, and B. Fischer, "Estimation of organ motion from 4D CT for 4D radiation therapy planning of lung cancer," in *Medical Image Computing and Computer-Assisted Intervention MICCAI'2004*, Lecture Notes in Computer Science, (Springer-Verlag, Berlin, 2004), Vol. 3217, pp. 1017–1024.

²⁶ L. Fan and C. W. Chen, "Integrated approach to 3D warping and registration from lung images," in *Proc. SPIE Developments in X-Ray Tomography II*, edited by U. Bonse, 1999, Vol. 3772, pp. 24–35.

²⁷ L. Fan, C. W. Chen, J. M. Reinhardt, and E. A. Hoffman, "Evaluation and application of 3D lung warping and registration model using HRCT images," in *SPIE Medical Imaging*, San Diego, CA, 2001, Vol. 4321, pp. 234–243.

²⁸ M. Betke, H. Hong, D. Thomas, C. Prince, and J. P. Ko, "Landmark detection in the chest and registration of lung surfaces with an application to nodule registration," *Med. Image Anal.* **7**, 265–281 (2003).

²⁹ L. Weruaga, J. Morales, L. Nunez, and R. Verdu, "Estimating volumetric motion in thorax with parametric matching constraints," *IEEE Trans. Med. Imaging* **22**, 766–772 (2003).

- ³⁰W. Lu, M. L. Chen, G. H. Olivera, K. J. Ruchala, and T. R. Mackie, "Fast free-form deformable registration via calculus of variations," *Phys. Med. Biol.* **49**, 3067–3087 (2004).
- ³¹T. Guerrero, G. Zhang, T. C. Huang, and K. P. Lin, "Intrathoracic tumor motion estimation from CT imaging using the 3D optical flow method," *Phys. Med. Biol.* **49**, 4147–4161 (2004).
- ³²T. A. Sundaram and J. C. Gee, "Towards a model of lung biomechanics: pulmonary kinematics via registration of serial lung images," *Med. Image Anal.* **9**, 254–237 (2005).
- ³³J. W. Wong, M. B. Sharpe, D. A. Jaffray, V. R. Kini, J. M. Robertson, J. S. Stromberg, and A. A. Martinez, "The use of active breathing control (ABC) to reduce margin for breathing motion," *Int. J. Radiat. Oncol., Biol., Phys.* **44**, 911–919 (1999).
- ³⁴P. A. Viola and W. M. Wells, "Alignment by maximization of Mutual Information," *Int. J. Comput. Vis.* **24**, 137–154 (1997).
- ³⁵F. Maes, A. Collignon, D. Vandermeulen, G. Marchal, and P. Suetens, "Multimodality image registration by maximization of mutual information," *IEEE Trans. Med. Imaging* **16**, 187–198 (1997).
- ³⁶J. Milic-Emili, J. A. Henderson, M. B. Dolovich, D. Trop, and K. Kaneko, "Regional distribution of inspired gas in the lung," *J. Appl. Physiol.* **21**, 749–759 (1966).
- ³⁷S. Monfraix, S. Bayat, L. Porra, G. Berruyer, C. Nemoz, W. Thomlinson, P. Suortti, and A. R. A. Sovijärvi, "Quantitative measurement of regional lung gas volume by synchrotron radiation computed tomography" *Phys. Med. Biol.* **50**, 1–11 (2005).
- ³⁸X. Pennec, P. Cachier, and N. Ayache, "Understanding the demon's algorithm: 3D non-rigid registration by gradient descent," in *Medical Image Computing and Computer-Assisted Intervention MICCAI'99*, Cambridge, UK, Lecture Notes in Computer Science, edited by C. Taylor and A. Colschesteher (Springer-Verlag, Berlin, 1999), Vol. 1679, pp. 597–605.
- ³⁹P. Cachier and N. Ayache, "Isotropic energies, filters and splines for vectorial regularization," *J. Math. Imaging Vision* **20**, 251–265 (2004).
- ⁴⁰V. Boldea, D. Sarrut, and C. Carrie, "Comparison of 3D dense deformable registration methods for breath-hold reproducibility study in radiotherapy," in *SPIE Medical Imaging: Visualization, Image-Guided Procedures, and Display*, 2005, Vol. 5747, pp. 222–230.
- ⁴¹C. Chef'd'Hotel, G. Hermosillo, and O. Faugeras, "A variational approach to multi-modal image matching," in *Proceedings of the IEEE Workshop on Variational and Level Set Methods (VLSM'01)*, Washington, DC, (IEEE Computer Society, Washington, D.C., 2001).
- ⁴²R. Deriche, Recursively implementing the Gaussian and its derivatives. Technical Report 1893, INRIA, April 1993, <http://www.inria.fr/rrrt/rr-1893.html>.
- ⁴³Y. Seppenwoolde, H. Shirato, K. Kitamura, S. Shimizu, M. van Herk, and J. V. Lebesque, "Precise and real-time measurement of 3D tumor motion in lung due to breathing and heartbeat, measured during radiotherapy," *Int. J. Radiat. Oncol., Biol., Phys.* **53**, 822–834 (2002).
- ⁴⁴D. Rey, G. Subsol, H. Delingette, and N. Ayache, "Automatic detection and segmentation of evolving processes in 3D medical images: Application to multiple sclerosis," *Med. Image Anal.* **6**, 163–179 (2002).
- ⁴⁵M. Engelsman, G. C. Sharp, T. Bortfeld, and H. Shirato, "How much margins reduction is possible through gating or breath hold," *Phys. Med. Biol.* **50**, 477–490 (2005).